

Journal of Fluid Mechanics

<http://journals.cambridge.org/FLM>

Additional services for *Journal of Fluid Mechanics*:

Email alerts: [Click here](#)

Subscriptions: [Click here](#)

Commercial reprints: [Click here](#)

Terms of use : [Click here](#)



Particle image velocimetry study of fractal-generated turbulence

R. Gomes-Fernandes, B. Ganapathisubramani and J. C. Vassilicos

Journal of Fluid Mechanics / *FirstView* Article / September 2012, pp 1 - 31

DOI: 10.1017/jfm.2012.394, Published online:

Link to this article: http://journals.cambridge.org/abstract_S0022112012003941

How to cite this article:

R. Gomes-Fernandes, B. Ganapathisubramani and J. C. Vassilicos Particle image velocimetry study of fractal-generated turbulence. Journal of Fluid Mechanics, Available on CJO doi:10.1017/jfm.2012.394

Request Permissions : [Click here](#)

Particle image velocimetry study of fractal-generated turbulence

R. Gomes-Fernandes^{1†}, B. Ganapathisubramani² and J. C. Vassilicos¹

¹ Department of Aeronautics, Imperial College London, London SW7 2AZ, UK

² Aerodynamics & Flight Mechanics Research Group, University of Southampton, Southampton SO17 1BJ, UK

(Received 18 April 2012; revised 31 July 2012; accepted 1 August 2012)

An experimental investigation involving space-filling fractal square grids is presented. The flow is documented using particle image velocimetry (PIV) in a water tunnel as opposed to previous experiments which mostly used hot-wire anemometry in wind tunnels. The experimental facility has non-negligible incoming free-stream turbulence (with 2.8% and 4.4% in the streamwise (u'/U) and spanwise (v'/U) directions, respectively) which presents a challenge in terms of comparison with previous wind tunnel results. An attempt to characterize the effects of the incoming free stream turbulence on the grid-generated turbulent flow is made and an improved wake-interaction length scale is proposed which enables the comparison of the present results with previous ones for both fractal square and regular grids. This length scale also proves to be a good estimator of the turbulence intensity peak location. Furthermore, a new turbulence intensity normalization capable of collapsing u'/U for various grids in various facilities is proposed. Comparison with previous experiments indicates good agreement in turbulence intensities, Taylor microscale, as well as various other quantities, if the improved wake-interaction length scale is used. Global and local isotropy of fractal-generated turbulence is assessed using the velocity gradients of the two-component (2C) two-dimensional (2D) PIV and compared with regular grid results. Finally, the PIV data appear to confirm the new dissipation behaviour previously observed in hot-wire measurements.

Key words: turbulence control, turbulence theory, wakes

1. Introduction

The study of turbulent flows originating from a fractal object obstructing a steady laminar stream started with Queiros-Conde & Vassilicos (2001) and Staicu *et al.* (2003) who took turbulence measurements in the wake of three-dimensional fractal branching tree-like objects. This was followed by some early fractal/multiscale-forced turbulence simulations by Mazzi, Okkels & Vassilicos (2002), Biferale *et al.* (2004) and Mazzi & Vassilicos (2004) and, after a few years, led to the first ever study of turbulence generated by planar fractal/multiscale grids (Hurst & Vassilicos 2007). Hurst & Vassilicos (2007) experimented with three different families of planar fractal grids: fractal cross-grids, fractal I-grids and fractal square grids (see figure 2 for the latter). They tried a total of 21 grids and reported unusual/unconventional properties

† Email address for correspondence: r.g.fernandes@imperial.ac.uk

only for their fractal square grids. As a result, the majority of subsequent studies of fractal-grid-generated turbulence have concentrated on fractal square grids (Seoud & Vassilicos 2007; Nagata *et al.* 2008*a,b*; Laizet, Lamballais & Vassilicos 2010; Mazellier & Vassilicos 2010; Stresing *et al.* 2010; Suzuki *et al.* 2010; Discetti *et al.* 2011; Laizet & Vassilicos 2011; Valente & Vassilicos 2011*a,b*; Laizet *et al.* 2012; Laizet & Vassilicos 2012). Even so, there have been a couple of studies which used multiscale/fractal cross-grids to enhance the Reynolds number (Geipel, Goh & Lindstedt 2010; Kinzel *et al.* 2011) and one set of high-quality measurements very far downstream of regular and multiscale cross-grids which has provided the most compelling data to date demonstrating the far downstream dependence of turbulence decay on inlet conditions (see Valente & Vassilicos 2012*a*) as originally proposed by George (1992). The measurements of pressure drop across planar fractal grids of Hurst & Vassilicos (2007) also motivated Aly, Chong, Nicolleau & Beck (2010), Nicolleau, Salim & Nowakowski (2011) and Zheng, Nicolleau & Qin (2012) to study the pressure drop across fractal-shaped orifices in turbulent pipe flows. Kang, Dennis & Meneveau (2011) measured drag forces on fractal Sierpinski carpets and triangles which look very similar to some of the fractal-shaped orifices used by Aly *et al.* (2010) and Nicolleau *et al.* (2011). Anderson & Meneveau (2011) studied and modelled flows over fractal-like multiscale surfaces.

The planar fractal I-grids introduced by Hurst & Vassilicos (2007) are two-dimensional analogues of the three-dimensional fractal branching tree-like structures used by Queiros-Conde & Vassilicos (2001). Whereas there has been no study of turbulence generated by fractal I grids since Hurst & Vassilicos (2007) (except for Mazellier & Vassilicos 2008 who used fractal I grid and fractal cross-grid data by Hurst & Vassilicos 2007 in their demonstration of the inlet-condition dependence of the turbulence dissipation constant), there has been some work starting with Chester, Meneveau & Parlange (2007) and Chester & Meneveau (2007) on fractal trees which are not dissimilar to the fractal I trees of Queiros-Conde & Vassilicos (2001). The focus of that work has been on the calculation of drag forces using renormalized numerical simulation to model the drag of unresolved branches of the fractal tree. More recently, particle image velocimetry (PIV) measurements were carried out in the near wake of a fractal-like tree demonstrating the importance of the tree's multiscale structure for the actual modelling of the flow (Bai, Meneveau & Katz 2012).

One of the motivations of the original experiments by Queiros-Conde & Vassilicos (2001) and of the early simulations by Mazzi & Vassilicos (2004), but also of much of the hot-wire anemometry (HWA) work which followed using fractal square grids (Seoud & Vassilicos 2007; Mazellier & Vassilicos 2010; Valente & Vassilicos 2011*a,b*), was to generate hitherto unexplored turbulent flow conditions where the high-Reynolds-number scaling of the kinetic energy dissipation ϵ might be significantly different from the conventional $\epsilon \sim K^{3/2}/L$ (where K and L are, respectively, the turbulent kinetic energy and some local correlation length scale). This scaling is referred to as ‘one of the cornerstone assumptions of turbulence theory’ by Tennekes & Lumley (1972), and Batchelor (1953) comments that it suggests ‘that energy transfer occurs chiefly as a result of inertial interactions of wavenumbers of the same order of magnitude’. Interestingly, Doering & Foias (2002) rigorously proved from the incompressible Navier–Stokes equations that periodic and statistically stationary body-forced three-dimensional turbulence is such that $\epsilon \leq c_1 \nu K/l^2 + c_2 K^{3/2}/l$ where ν is the kinematic viscosity, c_1 , c_2 are dimensionless Reynolds-number-independent coefficients and l is the longest length scale in the applied forcing assumed square-integrable. In the case where the body forcing is not square-integrable,

Cheskidov & Doering (2007) proved that the upper bound on ϵ may increase with increasing Reynolds number as indeed observed in the direct numerical simulations (DNS) of Mazzi & Vassilicos (2004) who investigated the behaviour of periodic and statistically stationary three-dimensional incompressible turbulence subjected to power-law multiscale/broadband body forcing. This was the first instance of an observed dramatic deviation from $\epsilon \sim K^{3/2}/L$ in a turbulent flow, albeit one in a computer. DNS of periodic fractal/broadband-forced turbulence were subsequently taken up by Kuczaj & Geurts (2006) and Kuczaj, Geurts & McComb (2006).

When describing Kolmogorov's universal equilibrium hypotheses, Batchelor (1953) stresses their clear implication that 'all turbulent motions – decaying homogeneous turbulence, flow in a pipe under pressure, flow in a boundary layer, turbulent wakes, flow in a fluid with density stratification, etc. – are such that at sufficiently large Reynolds number the motions associated with the small-scales have a common statistical form'. In particular, the closely related Reynolds-number-independent scaling $\epsilon \sim K^{3/2}/L$ is indeed customarily used in the modelling of many different turbulent flows including wakes, jets and shear layers (Townsend 1956), decaying homogeneous turbulence (Batchelor 1953; Valente & Vassilicos 2011a), stratified turbulence (Hopfinger & Toly 1976) and even models of the intermediate inertial layer in wall turbulence (e.g. Pope 2000; Dallas, Vassilicos & Hewitt 2009).

Assuming that the turbulence structure is isotropic, Taylor (1935) showed that $\epsilon = 15\nu u'^2/\lambda^2$ where λ is the Taylor microscale and u' the root-mean-square (r.m.s.) velocity fluctuation. In isotropic turbulence $\epsilon \sim K^{3/2}/L$ becomes $\epsilon = C_\epsilon u'^{3/2}/L$ where L is the longitudinal integral length scale and C_ϵ is a dimensionless constant independent of Reynolds number, time and spatial position. It is trivial to check that $\epsilon = C_\epsilon u'^{3/2}/L$ is equivalent to $15L/\lambda = C_\epsilon Re_\lambda$, where Re_λ is Reynolds number based on the Taylor microscale. The main discovery made by Seoud & Vassilicos (2007), Mazellier & Vassilicos (2010) and Valente & Vassilicos (2011a,b) is that a significantly large region exists in the lee of fractal square grids where the turbulence is approximately isotropic and where L/λ remains constant as Re_λ decays, hence seriously violating $15L/\lambda = C_\epsilon Re_\lambda$ and $\epsilon = C_\epsilon u'^{3/2}/L$ with C_ϵ constant. Instead, these authors observed that $C_\epsilon \sim 1/Re_\lambda$ and that C_ϵ and L/λ are increasing functions of a global Reynolds number defined by the inlet conditions (as opposed to Re_λ which is a local turbulence Reynolds number). The importance of a global inlet Reynolds number had previously been pointed out by George (1992), though not specifically for turbulence generated by fractal square grids.

Mazellier & Vassilicos (2010) introduced the wake-interaction length scale x_* which they used to define the streamwise boundary between two important regions: the region closer to the fractal square grid where turbulence is highly anisotropic, non-Gaussian and being produced inhomogeneously; and the region further downstream where the turbulence is approximately isotropic, Gaussian and decays without being significantly produced. Laizet & Vassilicos (2011) performed a DNS of turbulent flows generated by fractal square grids which confirmed the existence of these two adjacent regions. $C_\epsilon \sim 1/Re_\lambda$ and $L/\lambda \approx \text{const}$ during Re_λ -decay hold in a significant region around the centreline from less than about $x_*/2$ from the grid up to an *a priori* streamwise distance $x_e > x_*/2$ which has yet to be determined. Mazellier & Vassilicos (2010) also showed that the constant value taken by L/λ during Re_λ -decay is in fact an increasing function of the inlet velocity, U_∞ .

Valente & Vassilicos (2012b) applied the wake-interaction length scale to the analysis of turbulence generated by regular grids and found a hitherto largely

unexplored region between approximately $x_*/2$ and $x_e \approx 2x_*$ where $C_\epsilon \sim Re_M^{1/2}/Re_\lambda$ and $L/\lambda \sim Re_M^{1/2}$ independently of Re_λ during Re_λ -decay ($Re_M \equiv U_\infty M/\nu$ is the inlet (global) Reynolds number defined in terms of the inlet velocity U_∞ and the grid mesh size M). $C_\epsilon \sim 1/Re_\lambda$ is therefore not unique to fractal square grids, thus now raising the important question relating to the range of its validity and perhaps even universal presence in appropriately defined regions existing in a wide range of turbulent flows.

In this paper we investigate the potential universality of $C_\epsilon \sim 1/Re_\lambda$ and $L/\lambda \sim \text{const}$ during Re_λ -decay in two ways. Firstly we do our experiments in water whereas the experiments of Seoud & Vassilicos (2007), Mazellier & Vassilicos (2010) and Valente & Vassilicos (2011a,b, 2012b) were all done in wind tunnels. In this way we can, in principle, match inlet Reynolds numbers between water and air by reducing both U_∞ and ν by a factor of 10 with respect to the air and compare results. More importantly, however, we use a water flume with significant inlet free-stream turbulence intensity. Even though we use fractal square grids which are very closely matched to those used by Seoud & Vassilicos (2007) and Mazellier & Vassilicos (2010) (one of which was also used by Valente & Vassilicos 2011a,b), the inlet turbulence means that our water flow is potentially significantly different from the air flows of these authors even at similar mean inlet Reynolds numbers.

Detecting $C_\epsilon \sim 1/Re_\lambda$ and $L/\lambda \sim \text{const}$ during Re_λ -decay requires properly defining the region where they hold. In this paper we modify and generalize the definition of the wake-interaction length scale to take into account the influence of inlet free-stream turbulence. In doing so, we are also led to propose a scaling for the centreline turbulence intensity and its streamwise profile. Our new scaling collapses data from different Reynolds numbers, different inlet free-stream turbulence levels, two different working fluids, various fractal square grids and three regular grids. This scaling is useful for much more than just defining the start of the region where $C_\epsilon \sim 1/Re_\lambda$, Re_λ is high and the turbulence energy spectrum is a broad power-law with exponent close to $-5/3$. This scaling can be of pivotal importance in the design of multiscale/fractal grids for applications to efficient mixing and scalar transfer (Nagata *et al.* 2008b; Laizet & Vassilicos 2012), lean premixed combustion (Geipel *et al.* 2010), noise reduction in general and fractal spoilers in particular (Laizet *et al.* 2012; Nedic *et al.* 2012) and fractal fences (Keylock *et al.* 2012).

To our knowledge there have only been three PIV studies of fractal-generated flows to date, Suzuki *et al.* (2010), Discetti *et al.* (2011) and Bai *et al.* (2012). Of these, the first two are PIV studies of turbulence generated by fractal-square grids. There is therefore a pressing need for more PIV studies of such flows and the present paper reports on such a new study. Suzuki *et al.* (2010) looked at high-Schmidt-number mixing of passive scalar in turbulence generated by regular and fractal square grids using PIV together with planar laser-induced fluorescence (PLIF). They reported very significant stirring and scalar transfer enhancement by the fractal square grid. Discetti *et al.* (2011) tested the ability of stereoscopic PIV to measure relatively low turbulence intensity flows (where noise can dominate the signal) using turbulence generated by a fractal square grid. They found that the noise is a problem far downstream where the turbulence has decreased too much in intensity but PIV is nevertheless capable of detecting many of the flow features reported by Hurst & Vassilicos (2007), Seoud & Vassilicos (2007) and Mazellier & Vassilicos (2010). PIV is therefore well suited to the nearer field of grid-generated turbulence and Cardesa-Dueñas, Nickels & Dawson (2012) has already conducted an extensive such study using square-bar and round-bar regular grids in a water channel. We carry out planar PIV measurements of three planar space-filling fractal square grids of the same, low, blockage ratio which are

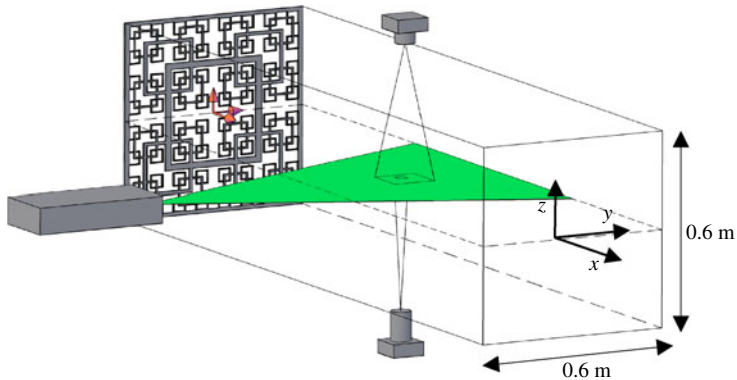


FIGURE 1. (Colour online) Experimental setup.

very similar to those used by Mazellier & Vassilicos (2010). In the absence of a grid obstruction, the facility we use has a background free-stream turbulence intensity of 2.8% in the streamwise and 4.4% in the lateral directions. An assessment of both large-scale and small-scale isotropy in the presence of a fractal square grid (shown below in figure 2) is therefore important, both because of the anisotropy of the inlet turbulence and because of the importance of isotropy for the calculation and scaling of ϵ . Such an assessment is therefore offered in this present paper. We also use HWA data by Groth & Johansson (1988) and Mazellier & Vassilicos (2010) and PIV data by Cardesa-Dueñas *et al.* (2012) for comparison.

This paper is divided into five sections. In the following section, we describe our experimental facility and provide details of the flow, PIV processing and carry out a brief uncertainty analysis. In § 3, we show the procedure involved in determination of kinetic energy dissipation and use this to identify the resolution of our measurements. Section 4 contains detailed results from our study. We present the new wake-interaction length scale and utilize it to collapse the current data with all previously presented results in the literature. We also present various turbulence statistics and scales including local and global isotropy metrics, Taylor microscales, integral scales and dissipation scaling. Finally, we present our conclusions in § 5.

2. Experimental details

2.1. Experimental facility

Experiments are carried out in a recirculating water tunnel, and a schematic of the test section is shown in figure 1. The tunnel cross-section is rectangular, 0.6 m wide and 0.7 m deep, and the test section is 9 m long. Because it is an open surface water tunnel, a roof made of transparent Perspex is installed to prevent any velocity fluctuations arising from waves formed at the surface. This device reduces the tunnel depth from 0.7 to 0.6 m, making the cross-section geometry square, which is similar to the wind tunnel measurements made previously (Hurst & Vassilicos 2007; Seoud & Vassilicos 2007; Mazellier & Vassilicos 2010; Valente & Vassilicos 2011a).

Optical access is provided through the sidewalls, bottom and roof. The fractal grid is positioned immediately downstream of a 4.5:1 contraction. The flow entering the contraction of the water tunnel passes through one honeycomb and one screen. Consequently, the free-stream turbulence intensity in the absence of a turbulence-

Case	U_∞ (m s ⁻¹)	Re_0			Re_{L_0}
		SFG8	SFG13	SFG17	
A	0.48	8400	10 000	11 200	144 900
B	0.59	10 300	12 300	13 800	178 100
C	0.69	12 000	14 400	16 000	208 300

TABLE 1. Free-stream velocities and Re for the three experimental cases. SFG8, SFG13 and SFG17 are the three grids tested. Re_0 and Re_{L_0} are the Reynolds numbers based on the thickness t_0 and on the distance L_0 between the thickest bars, respectively (see figure 2 for geometrical details), i.e. $Re_0 = U_\infty t_0 / \nu$ and $Re_{L_0} = U_\infty L_0 / \nu$.

generating grid is up to 2.8% for the streamwise fluctuating velocity u and 4.4% for the spanwise fluctuating velocity v . These estimates were obtained by carrying out PIV measurements immediately downstream of the contraction without the fractal grid. The turbulence intensity in the streamwise direction (u'/U) peaks 1.8 m downstream of the grid with a value of 3.2% whereas the turbulence intensity in the spanwise direction (v'/U) always decreases and has a value of 3.7% at the same distance downstream, 1.8 m.

The presence of non-negligible free-stream turbulence presents an opportunity. On the one hand, it might affect results in a way that might not allow comparison with previous wind tunnel low inlet free-stream turbulence experiments. On the other hand, if the fractal grids, in some sense, ‘break’ the incoming turbulence and if the turbulence behaves thereafter as in previous experiments, that would be a significant result.

It must be noted that most of the analysis carried out in this study requires access to the inlet speed (U_∞). This speed is used to normalize various quantities in subsequent sections. However, we are unable to measure the inlet speed upstream of the grid due to lack of optical access. Therefore, it is not possible to compare data from the wind tunnel experiments with the present one based only, for example, on a global Reynolds number $Re_0 = f(U_\infty, l, \nu)$ (where l is an appropriate length scale characteristic of the grid and ν is the kinematic viscosity of the fluid). On the other hand, we do measure the flow rate. We use this flow rate to evaluate an estimate for the inlet speed. This estimated free-stream speed allows us to compare the results from different experiments. The free-stream velocity, U_∞ , in our study is defined as the mean velocity of the tunnel 0.3 m downstream of the grid position when the grid is not positioned in place. The power is kept constant and the grid is positioned in place before the measurements. Three different power settings were used resulting in three different experimental cases as shown in table 1.

2.2. Fractal grid geometry

For the present work, space-filling fractal square grids (SFG) with four ‘fractal iterations’ (N) are used. Three quantitatively different (but qualitatively identical) geometries are employed where only the thickness ratio (t_r) is changed; t_r is the ratio between the thickness of the thickest bar (t_0) and of the thinnest bar (t_{min}), see figure 2. For the present study three different t_r values are used: 8.5, 13 and 17 as in Mazellier & Vassilicos (2010). L_0 , the distance between the thickest bars, and the blockage ratio, σ , are both kept constant and are the same for all three grids. Table 2 summarizes

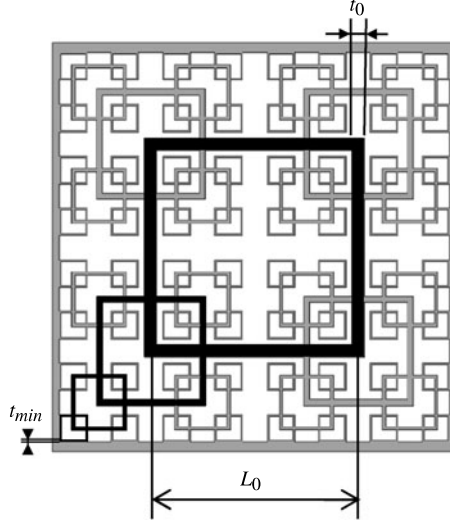


FIGURE 2. Space filling square fractal grid (SFG) geometry. The ‘fractal iterations’ parameter (N) is the number the square shape is repeated with different scales.

Grid	SFG8	SFG13	SFG17
N	4	4	4
t_r	8.5	13.0	17.0
t_0 (mm)	17.5	21.0	23.5
t_{min} (mm)	2.1	1.6	1.4
L_0 (mm)	302.9	303.2	303.3
σ	25.3	25.0	25.0

TABLE 2. Fractal grids geometry details.

the various grid geometries used in this study. The lengths L_1 , L_2 and L_3 of the three iterations of bars shorter than L_0 are $L_3 = (1/2)L_2 = (1/4)L_1 = (1/8)L_0$. The spanwise thicknesses t_1 , t_2 and t_3 of these bars are $t_3 = t_r^{1/3}t_2 = t_r^{2/3}t_1 = t_r t_0$. The thickness of all bars in the streamwise direction (denoted chord from this point onwards) is 5 mm.

2.3. Experimental technique

The flow velocity is measured with two-dimensional (2D), two-component (2C) PIV. The flow is seeded with polyamide 12 powder which consists of particles of $7 \mu\text{m}$ mean diameter and 1.1 specific gravity. The response time (τ_p) of the seed particles is estimated to be $0.3 \mu\text{s}$. The Stokes number $St = \tau_p/\tau_F$ (where τ_F is the characteristic time scale of the smallest eddies) must be less than 1 for the particles to faithfully follow the flow. The characteristic time considered here is the Kolmogorov time scale $\tau_\eta = \sqrt{\nu/\epsilon}$ (where ν is the kinematic viscosity of water and ϵ is the kinetic energy dissipation) which is approximately 25 ms. This results in a Stokes number of 1.1×10^{-5} and indicates that particles track the velocity fluctuations in the flow fairly well.

The flow is illuminated by a double-pulsed Nd:YAG laser with a maximum energy output of $200 \text{ mJ pulse}^{-1}$ (Litron Nano series). The laser is set at a sampling frequency of 1.04 Hz in order to record statistically independent images. The laser light sheet is formed after the beam has passed through a spherical lens to converge the sheet into a minimum thickness of around 1.2 mm at a point in the middle of the measurement plane. After the spherical lens, a cylindrical lens is placed in order to spread the light sheet and illuminate the desired field of view, thus creating a horizontal light sheet as seen in figure 1. The light sheet plane is in the horizontal mid-plane of the channel.

The PIV images are recorded by two CCD cameras (TSI POWERVIEWTM Plus) with 2048×2048 pixel resolution. As seen in figure 1, the cameras are placed looking perpendicular to the light sheet from the top and bottom (a technique first introduced by Buxton 2011). The top camera images a large field of view (LFV) whereas the bottom camera images a smaller field of view (SFV) contained within the larger one. The two cameras are synchronized together with the laser sheet pulse at 1.04 Hz. Both cameras are fitted with a Sigma 105 mm $f/2.8$ EX DG Macro lens set with $f\#$ of 4. A minimal effect of peak locking was found for these experimental conditions.

Since the two cameras are operating simultaneously at different magnifications, the pixel displacement is higher in the SFV camera (bottom one) than in the LFV one. Therefore, a balance has to be reached between a minimum pixel displacement in the top camera, for data accuracy, and a maximum pixel displacement for the bottom camera which limits the out-of-plane particle motion and hence any loss of correlation. This balance is achieved by changing δt , the time between two image frames and it depends on the turbulent intensity in the flow. Hence, for regions close to the turbulence intensity peak the pixel displacement is roughly 6/28 px (top camera/bottom camera) and 8/35 px for the turbulence decaying region.

The calibration target is printed on a transparent sheet as a matrix of dots of 1.5 mm diameter spaced 20 mm from each other for the LFV and a matrix of dots of 0.2 mm diameter spaced 4 mm from each other for the SFV. The displacement vectors are mapped from the image plane to the object plane via a third-order polynomial function (Soloff, Adrian & Liu 1997) to account for any aberrations due to the lenses, Perspex or glass medium and water.

The PIV analysis is done using a commercial PIV software (DaVis 8.0, LaVision). There are 10 stations in total where for each grid, free-stream velocity, camera and station, a total of 1500 images are acquired. The first station is located 0.30 m downstream of the grid and the remaining stations are spaced 0.50 m from each other with the exception of station 8 which is 0.35 m downstream of station 7 due to constraints related to the water tunnel's optical access. The vector fields are obtained by processing the PIV images using a recursive cross-correlation engine with a final interrogation window of size 32×32 pixels with 50% overlap.

Figures 3 and 4 show two examples of PIV results from the LFV and SFV, respectively, for the first station of measurements, 0.3 m downstream of the grid. The grid wakes are noticeable from the averaged flow field (figure 3) and an example of the turbulent flow field is shown in the instantaneous fluctuation velocity field (figure 4). The SFV is represented by the dashed lines in the LFV in figure 3.

Table 3 provides a summary of the main experimental parameters.

2.4. Uncertainty analysis

There are two different main sources of uncertainty in the experimental results of turbulent quantities. One arises from the statistical sampling of the data and the other

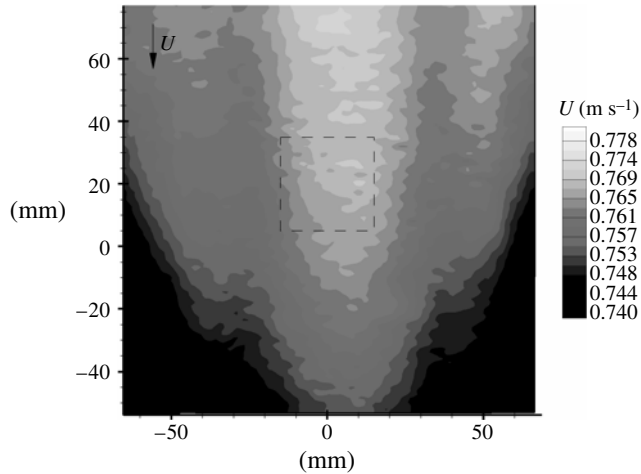


FIGURE 3. Averaged streamwise velocity field for SFG17, case B, at the first station of measurements (0.3 m downstream of the grid) for the large field of view (LFV).

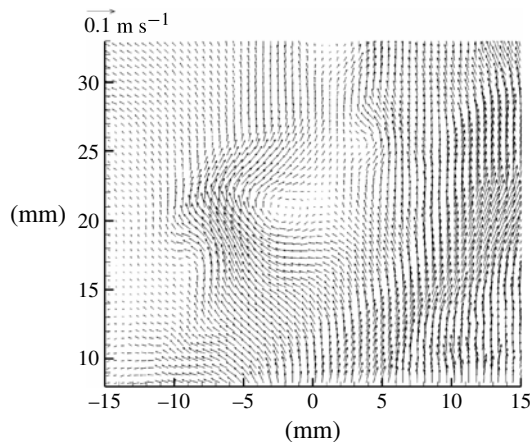


FIGURE 4. Fluctuating velocity field for SFG17, case B, at the first station of measurements (0.3 m downstream of the grid) for the small field of view (SFV). Only half of the vector count is shown here.

from the PIV random error. For high turbulence level flows, the PIV random error is substantially smaller than the turbulence fluctuations and, therefore, it is usual to consider the estimation of the latter as the only source of uncertainty. The PIV random error is estimated by computing the variance of the velocity fluctuations by extrapolating the correlation function to where the distance of the two points is zero and comparing it with the value calculated using the normal procedure for one-point statistics (see figure 9.17 of Adrian & Westerweel 2011). In the present experiment u'^2 , which is the variance of streamwise velocity fluctuations, is $O(10^2)$ bigger than the mean-squared amplitude of the PIV random error, σ_ϵ^2 . Hence, only statistical sampling analysis is performed to estimate the measurement uncertainty.

Seeding	Type	Polyamide 12 powder
	Specific gravity	1.1
	Diameter	7 μm
Light sheet	Laser type	Nd:YAG
	Maximum energy	200 mJ pulse ⁻¹
	Wave length	532 nm
	Thickness	1.2 mm
Camera	Type	CCD
	Resolution	2048 \times 2048 px
	Pixel size	7.4 μm
	Repetition rate	1.04 Hz
	Lens focal length	105 mm
	f#	4
Imaging	Image magnification	0.45 (SFV)
		0.10 (LFV)
	Viewing area	30 mm \times 30 mm (SFV) 130 mm \times 130 mm (LFV)
PIV analysis	Interrogation area (IA)	32 \times 32 px
	Overlap IA	50 %
	Approximate resolution	0.53 mm \times 0.53 mm \times 1.2 mm (SFV) 1.3 mm \times 1.3 mm \times 1.2 mm (LFV)

TABLE 3. PIV experimental parameters.

Station	1	2	3	4	5	6	7	8	9	10
Rel. uncert. (\pm %)	11.4	13.9	7.2	6.4	6.7	7.0	7.0	7.9	7.3	7.5

TABLE 4. Relative uncertainties of u^2 for grid SFG13, case B.

Using a 95 % confidence interval, the true value of u^2 is within the interval $u^2 \pm 1.96\sqrt{s_{u^2}/N}$ where s_{u^2} is the variance of u^2 and N is the number of samples which is, in the present case, 1500. Table 4 shows the relative uncertainties, in terms of \pm percentage of u^2 , for grid SFG13, case B, which is representative of the level of the uncertainties for the other cases and grids in the present study and also are in line with what other researchers have found, such as Cardesa-Dueñas *et al.* (2012). The relative uncertainties presented in table 4 are computed for a single vector position and for each measurement station.

The velocity gradients are estimated using only the small field of view and, in order to reduce the statistical sampling uncertainty, the gradients are averaged across the whole field of view and the 1500 images, thus resulting in around 1.8×10^6 samples for each station. A de-noising procedure outlined by Tanaka & Eaton (2007) is used to obtain mean-square values of the gradients. Details of this procedure and its application to the data are discussed in § 3. Comparisons with previous studies at similar locations show good agreement between the PIV results and the hot-wire data (also see § 4.3).

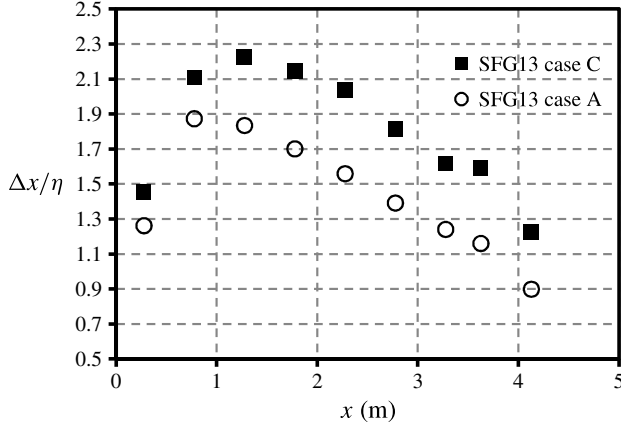


FIGURE 5. Comparison of the ratio of the distance between two velocity vectors in the SFV and the Kolmogorov microscale in relation to the position downstream of the grid and for cases A and C as shown in table 1. Note that the interrogation window size is twice the spacing between the vectors since we are using 50 % overlap.

3. Energy dissipation estimation

In order to estimate important parameters such as energy dissipation, and Taylor and Kolmogorov microscales it is necessary to compute mean-squared values of velocity gradients.

In particular, for energy dissipation, planar PIV provides a plane of velocity measurements where from the nine components of the velocity gradient, only four are directly computed or five if the compressibility equation is taken into account. Therefore, in this case, energy dissipation is estimated using the following equation, which is an approximation used for 2C 2D PIV results after Tanaka & Eaton (2007):

$$\epsilon \approx 3\nu \left(\overline{s_{11}^2} + \overline{s_{22}^2} \right) + 12\nu \overline{s_{12}^2}. \quad (3.1)$$

Here ϵ is the energy dissipation, ν is the fluid kinematic viscosity, $s_{ij} = ((\partial u_i / \partial x_j) + (\partial u_j / \partial x_i)) / 2$ is the strain rate of the velocity fluctuations and u_i is the velocity fluctuation. It is assumed that turbulence is locally isotropic, so $\overline{s_{33}^2} = (\overline{s_{11}^2} + \overline{s_{22}^2}) / 2$ and $\overline{s_{13}^2} = \overline{s_{23}^2} = \overline{s_{12}^2}$ (the overbar represents an ensemble average and we use it interchangeably with angle brackets, $\langle \rangle$). This ensemble average is a time average when we calculate quantities such as turbulence intensities at a point, but space and time averages when we calculate the mean square gradients).

Knowing the energy dissipation, it is now possible to estimate the Kolmogorov microscale $\eta = (\nu^3 / \epsilon)$. Figure 5 shows the behaviour of the Kolmogorov microscale in comparison with Δx , the distance between two velocity vectors in the SFV plane. This figure presents data for cases A and C which are related to the minimum and maximum inlet velocity, U_∞ , respectively.

Saarenrinne & Piirto (2000) demonstrated that for decreasing Δx the dissipation error increases exponentially due to the square of the fluctuation velocity gradient. Tanaka & Eaton (2007) proposed a method to correct the energy dissipation estimated by PIV which is best suited for $\eta / 10 < \Delta x < \eta / 2$ when 50 % overlap is used between interrogation windows. From figure 5 it is possible to see that the present case is not within the aforementioned range but, since there is noise in the data, it was chosen to

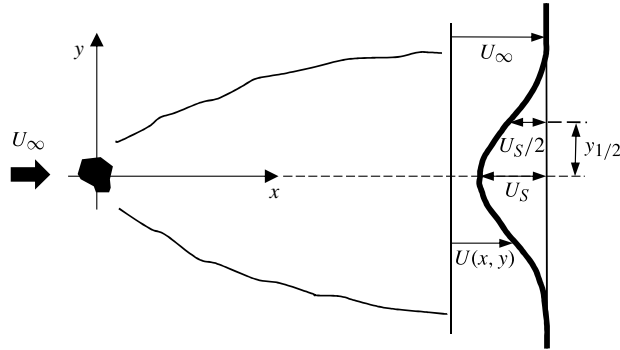


FIGURE 6. Important parameters defining the wake physics, after Wygnanski *et al.* (1986).

apply this method regardless. Hence, for the computation of quantities like $\overline{(\partial u_i / \partial x_j)^2}$, this correction was applied.

4. Results

4.1. Wake-interaction length scale

The wake-interaction length scale for fractal-generated turbulence was first defined by Mazellier & Vassilicos (2010) as

$$x_* = L_0^2 / t_0. \quad (4.1)$$

This parameter is proportional to the distance where the wakes of two bars of thickness t and separated by a distance L meet. In this case x_* is defined with L_0 and t_0 which are related to the thickest bars of the fractal grid. This wake-interaction length scale is useful for normalizing results related to fractal grids with different geometric characteristics. However, x_* does not take into account the effect of free-stream turbulence on the wake development. An attempt to improve the wake-interaction length scale is made in this section in order to be able to compare data from wind tunnel experiments (where free-stream turbulence is negligible) with the present water tunnel data where inlet free-stream turbulence is considerable.

When a self-preserving state is achieved behind a wake generator, the mean flow can be described using a characteristic velocity deficit and a wake width (see the schematic in figure 6). The velocity scale is chosen as the maximum wake deficit (U_S) and the wake width ($y_{1/2}$) is taken to be the half-width, i.e. the location where the velocity deficit is half its maximum value at a given streamwise location (see Wygnanski, Champagne & Marasli 1986).

Mazellier & Vassilicos (2010), following Townsend (1956), scaled $y_{1/2}$ with $\sqrt{t_0 x}$ and, by just considering the wake of the biggest bars (see figure 4a of Mazellier & Vassilicos 2010), defined the wake-interaction length scale, x_* , by $L_0 = y_{1/2} \propto \sqrt{t_0 x_*}$ thus leading to (4.1).

Figure 7(a) shows the streamwise turbulence intensity acquired from a hot-wire anemometer in a wind tunnel from Mazellier & Vassilicos (2010), together with PIV data from our water tunnel. It is seen that data do not collapse and the reason is mainly because (4.1) does not take into account the inlet free-stream turbulence present in the water tunnel. In order to take this into account a similar approach to

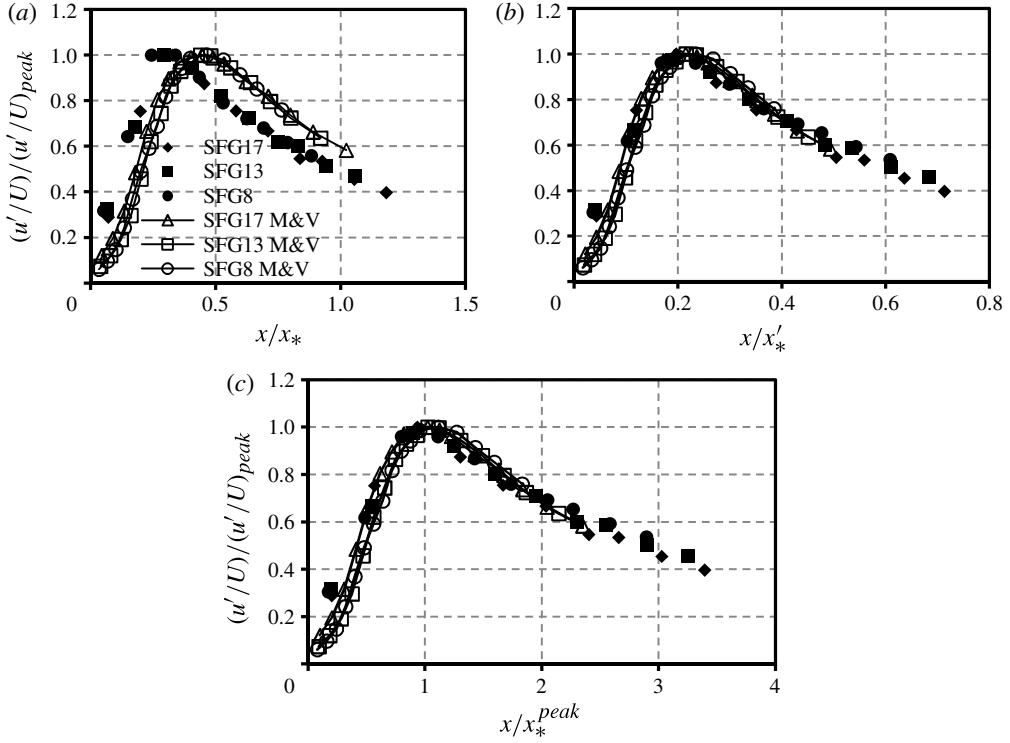


FIGURE 7. Streamwise evolution of the centreline turbulence intensity normalized by its maximum value for case B, is given as a function of x scaled by (a) x_* , (b) x'_* and (c) x_*^{peak} . Open symbols show data taken from figure 5 of Mazellier & Vassilicos (2010) (denoted throughout the figures as M&V).

the derivation of (4.1) can be made but using a more accurate description of the wake half-width development when free-stream turbulence is present.

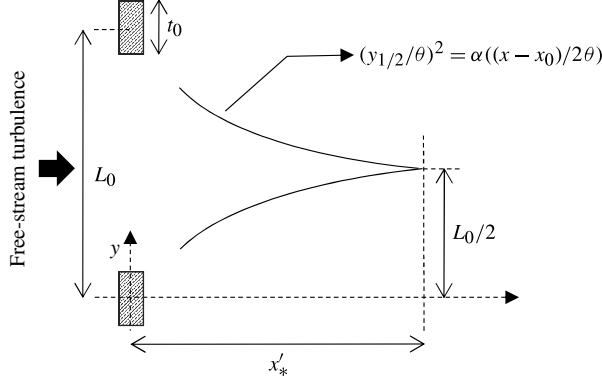
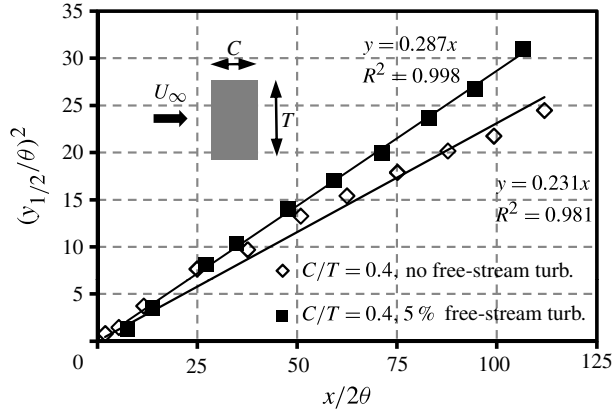
Symes & Fink (1977) studied the 2D wakes of circular and rectangular cylinders with and without free-stream turbulence and mapped their half-width scales. Therefore, it is possible to follow a similar approach as Mazellier & Vassilicos (2010) in determining a new interaction length scale but by taking into account the free-stream turbulence.

Results from Mazellier & Vassilicos (2010) and Valente & Vassilicos (2011a) show that their data collapse well with x_* which is based on the characteristics of the thickest bars. Consider therefore figure 8 which includes only the wakes of the thickest bars. Wygnanski *et al.* (1986) showed that self-similar small-deficit wake velocity and length scales, in the absence of a pressure gradient, vary as

$$\left(\frac{U_\infty}{U_s}\right)^2 \propto \left(\frac{x-x_0}{2\theta}\right), \quad \left(\frac{y_{1/2}}{\theta}\right)^2 \propto \left(\frac{x-x_0}{2\theta}\right) \quad (4.2)$$

where x_0 is the virtual origin and θ is the momentum thickness.

The results from Symes & Fink (1977) (see figure 9) allow us to drop the proportionality sign in (4.2) and model the development of the wake by the following

FIGURE 8. Wake schematic for the derivation of x'_* .FIGURE 9. Influence of external turbulence upon the development of the wake half-width, after Symes & Fink (1977), where C is the chord of a single bar and T its thickness.

behaviour:

$$\left(\frac{y_{1/2}}{\theta}\right)^2 = \alpha \left(\frac{x - x_0}{2\theta}\right) \quad (4.3)$$

where α is the parameter which takes into account the free-stream turbulence intensity and length scale. Because we are considering self-similar wakes, the distance downstream where the wakes meet is very much larger than the virtual origin. We therefore ignore the virtual origin x_0 and effectively set it equal to zero. The aim of (4.3) is just to determine a length scale proportional to the intersection of the two wakes (see figure 8) and not a very accurate value for it.

Figure 9 shows the streamwise growth of the wake half-width of a rectangular cylinder with 5% free-stream turbulence intensity and without free-stream turbulence. A linear trend-line based on (4.3) with $x_0 = 0$ is fitted to the data. We see that for data with inlet free-stream turbulence α is around 0.287 and for no inlet free-stream turbulence α is close to 0.231.

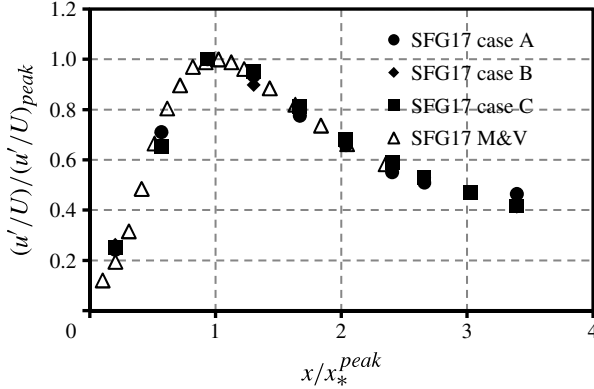


FIGURE 10. Turbulence intensity of the grid SFG17 normalized by its peak value in relation to the distance downstream normalized by x_*^{peak} for the three different cases studied in the present paper and for one case from Mazellier & Vassilicos (2010).

Now that the parameters for the equation of the wake development have been set, a similar approach to what was proposed to derive x_* (Mazellier & Vassilicos 2010) can be followed here based on figure 8. Relating the momentum thickness θ to the drag coefficient C_d via $\theta = C_d t_0 / 2$, the wakes meet at a distance x'_* where $y_{1/2} = L_0 / 2$:

$$x'_* = \frac{L_0^2}{\alpha C_d t_0}. \quad (4.4)$$

Figure 7(b) shows the centreline turbulence intensity in the wake of fractal grids with streamwise distance normalized by x'_* . Note that values of α of 0.231 and 0.287 are used for the data from the hot-wire experiments and the current study, respectively. The drag coefficients, C_d , for both data sets are taken from Bearman & Trueman (1972) and Nakamura & Tomonari (1976) for values without and with free-stream turbulence, respectively (see table 6 below).

It is possible to see from figure 7(b) that the collapse at positions where $x/x'_* > 0.4$ is not perfect. This is likely to be due to the fact that C_d and α in (4.4) were taken from references where the experimental conditions were not exactly the same as in the present study. Nevertheless, figure 7(b) is an improvement on figure 7(a) considering the difficulty of accounting for free-stream turbulence and the fact that we are comparing two different experimental facilities (water and wind tunnel) and two different experimental methods (PIV and hot-wire anemometry).

From figure 7(b) it is noticeable that the peak of turbulence intensity is located at $x/x'_* \approx 0.21$. This observation is based on the data of Mazellier & Vassilicos (2010) given that they captured the peak location better as they took measurements at more points downstream of the grid. According to their data the peak is located at $x/x'_* = 0.2 \pm 0.1$, 0.21 ± 0.1 and 0.23 ± 0.1 , for the three types of grid seen in figure 7(b). Hence, we choose the average of these values for a renormalization where a new variable x_*^{peak} is introduced as follows:

$$x_*^{peak} = \phi x'_* = 0.21 x'_* = 0.21 \frac{L_0^2}{\alpha C_d t_0} \quad (4.5)$$

where ϕ is the coefficient that multiplies expression (4.4) in order to get x_*^{peak} , $\phi = 0.21$ in figure 7(b). This change of variable results in the normalization in figure 7(c) where $x/x_*^{peak}=1$ marks the location of the turbulence intensity peak. From this point onwards, the downstream distance x for all data, unless stated otherwise, will be normalized by x_*^{peak} .

Figure 10 shows the turbulence intensity values of the grid SFG17 in relation to x/x_*^{peak} for the three different experimental cases studied here (see table 1) and for one case from Mazellier & Vassilicos (2010). It shows that there is practically no difference between them and, therefore, when dealing with turbulence intensities, only case B will be shown for brevity in the remainder of this paper.

Equation (4.5) provides an estimation of the turbulence intensity peak location but it should be used with caution, especially if applied to regular grid results, since this expression was derived based on the results of fractal grids. Note also that (4.5) includes an Re dependence of x_*^{peak} through the parameter C_d and, to some extent, through α , even though the behaviour of the latter parameter when Re is varied remains unclear. The grid cross-section geometry is also accounted for in (4.5) through C_d and α . This is a significant result as the grid chord (parameter C in figure 9) plays an important role in the wake growth and velocity deficit. Therefore, this chord length should be taken into account when designing grid turbulence experiments.

The present analysis considers the wakes from the biggest bars to be dominant and neglects the contributions of the smallest squares. This seems to be valid for values of t_r equal to and bigger than 8.5 which is the minimum t_r tested here. At sufficiently smaller values of t_r the thickness of the smallest squares becomes non-negligible and their wakes influence the location of the turbulence intensity peak as well as the turbulence intensity at this location as can be clearly seen in figure 39(a) from Hurst & Vassilicos (2007).

Finally, it must be noted that the values of α are taken from previous references and therefore may not exactly fit with the inlet free-stream turbulence in the current study. We would expect an even better collapse if α were calculated for our specific experimental conditions.

4.2. Turbulence intensity scaling

It has been shown in the previous section that the streamwise development of the turbulence intensity can be collapsed using x_*^{peak} , the wake-interaction length scale. However, this collapse also depends on the maximum value of turbulence intensity, which is used to normalize the turbulence intensity at all streamwise locations. Whilst the observation that turbulence intensities scale with the maximum turbulence intensity is not trivial (and was already used by Mazellier & Vassilicos 2010) it remains of little interest without a scaling relation for the maximum turbulence intensity itself. In this section, we introduce a scaling relation which allows us to estimate the maximum turbulence intensity for a given grid geometry and flow condition.

Consider the streamwise mean momentum equation of an isolated wake in the far-wake region (Pope 2000, p. 148),

$$U \frac{\partial U}{\partial x} = -\frac{\partial \overline{uv}}{\partial y} - \frac{\partial}{\partial x}(\overline{u^2} - \overline{v^2}) \quad (4.6)$$

where U is the mean velocity in the streamwise direction and u and v are the velocity fluctuation components in the x and y directions, respectively. It is possible to simplify (4.6) by making further assumptions. Firstly, the results of Antonia, Zhou & Romano (2002) and Eames, Jonsson & Johnson (2011) show that $\overline{v^2}$ can be related

to $\overline{u^2}$ via a constant value ξ since their behaviour with the streamwise distance is similar. Secondly, the Reynolds stress \overline{uv} is related to a self-similar function $g(\eta)$ via $\overline{uv} = U_S g(\eta)$ where $\eta = y/y_{1/2}(x)$ (see figure 6 for notation). Figure 7 from Wygnanski *et al.* (1986) shows that $\partial\overline{uv}/\partial y$ is zero at $\eta \approx 1$. We used $\eta = 1$ to derive the wake-interaction length scale in § 4.1 because the turbulence intensity at the centreline attains a maximum value where the two largest wakes intercept and their half-widths $y_{1/2}$ equal y . To derive the turbulence intensity scaling we evaluate (4.6) at $\eta = 1$ where $\partial\overline{uv}/\partial y = 0$. Hence, (4.6) can be re-written as

$$-U_{y_{1/2}} \frac{dU_{y_{1/2}}}{dx} = (1 - \xi) \frac{d\overline{u^2}_{y_{1/2}}}{dx} \quad (4.7)$$

where $\overline{u^2}_{y_{1/2}}$ is the mean of the streamwise velocity fluctuations squared and $U_{y_{1/2}}$ is the mean flow velocity, both at the wake half-width. Equation (4.7) can be integrated along the line where $\eta \approx 1$ which is given by (4.2) and is approximately $y \approx \gamma\sqrt{x}$. Equation (4.7) thus integrated yields

$$\oint_{s_0}^{\infty} \left(U_{y_{1/2}} \frac{dU_{y_{1/2}}}{dx} + (1 - \xi) \frac{d\overline{u^2}_{y_{1/2}}}{dx} \right) ds = 0 \quad (4.8)$$

where the integral is curvilinear along $y \approx \gamma\sqrt{x}$ and the variable of integration is denoted s and is related to x and y by $ds^2 = dx^2 + dy^2$. This can be translated to

$$\int_{x_0}^{\infty} \sqrt{1 + \frac{\gamma^2}{4x}} \frac{d}{dx} \left(\frac{U_{y_{1/2}}^2}{2} + (1 - \xi) \overline{u^2}_{y_{1/2}} \right) dx = 0. \quad (4.9)$$

The parameter γ is of $O(10^{-1})$ (see (4.3) and values of α from figure 9). In the region where $4x \gg \gamma^2$, the above equation simplifies to

$$\int_{x_0}^{\infty} \frac{d}{dx} \left(\frac{U_{y_{1/2}}^2}{2} + (1 - \xi) \overline{u^2}_{y_{1/2}} \right) dx = 0. \quad (4.10)$$

Integrating the above equation and assuming that as $x \rightarrow \infty$, $U_{y_{1/2}} \rightarrow U_{\infty}$ and $\overline{u^2}_{y_{1/2}} \rightarrow 0$, we obtain a relation for $\overline{u^2}_{y_{1/2}}$:

$$\overline{u^2}_{y_{1/2}} = \frac{(U_{\infty} - U_{y_{1/2}})^2}{2(1 - \xi)}. \quad (4.11)$$

It is well-established that the far-wake self-similar mean velocity profile of a turbulent wake is $f(\eta) = (U_{\infty} - U)/U_S$ (see Wygnanski *et al.* 1986). Utilizing this self-similar function in the above equation, we obtain the following relation between the velocity deficit and the turbulence intensity:

$$\overline{u^2}_{y_{1/2}} = \frac{(f(1)U_S)^2}{2(1 - \xi)}. \quad (4.12)$$

This relation is well-known (Tennekes & Lumley 1972) and its origin is perhaps now a bit clearer on the basis of the streamwise mean momentum equation.

According to (4.2), the wake velocity deficit scales with the momentum thickness of the flow, which in turn is related to the drag coefficient (C_d) and the thickness of the

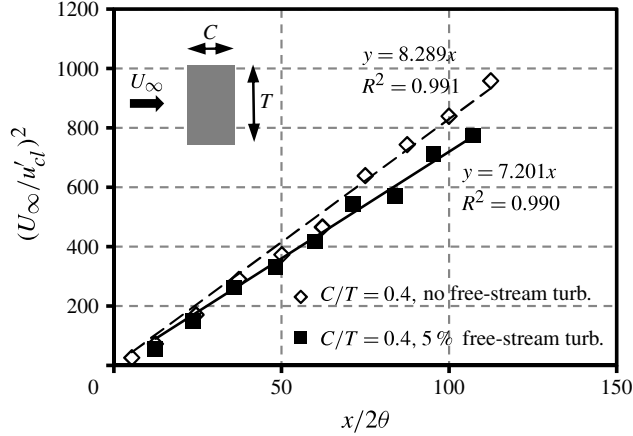


FIGURE 11. Influence of external turbulence upon the development of turbulence intensity at the wake centreline, after Symes & Fink (1977).

bar (t_0):

$$\left(\frac{U_\infty}{U_s}\right)^2 \propto \left(\frac{x - x_0}{C_d t_0}\right)^2. \quad (4.13)$$

The virtual origin (x_0) may be ignored to be consistent with our argument in §4.1. Thus far, all the relations have been derived for a laminar free stream. It is not trivial to account for the presence of free-stream turbulence. We utilize the experimental results from Symes & Fink (1977) to include the effects of free-stream turbulence on the maximum turbulence intensity. A new parameter β that relates the turbulence intensity at the wake centreline to the free-stream turbulence is introduced. Furthermore, it is assumed that this parameter β is essentially unchanged across the wake. Therefore, the value of β at half wake-width is taken to be the same as that for the wake centreline. Using (4.12) and (4.13) with $x_0 = 0$ and the parameter β the following relation is obtained:

$$\frac{U_\infty^2}{u_{y_{1/2}}^2} \propto \beta^2 \frac{x}{C_d t_0}. \quad (4.14)$$

Figure 11 shows a plot of the centreline turbulence intensity in the wake of a single bar of chord C and thickness T as a function of streamwise distance for different free-stream turbulence levels (the data are taken from Symes & Fink 1977). Note that the inverse of the squared turbulence intensity (U^2/u^2) is plotted as a function of streamwise distance x from the wake-generating obstruction. It can be seen that in the case of a laminar free stream the value of β^2 is 8.3. However, when the free-stream turbulence level increases to 5% then β^2 reduces to a value of 7.2. We use this value of β^2 for the data obtained in our study.

It is important to stress that the results from figure 7(a-c) consist of the turbulence intensity calculated with respect to the mean velocity at each station whereas in relation (4.13) the velocity fluctuations are normalized by the free-stream velocity (U_∞). Therefore, in order to apply (4.13), figure 12 first shows the present experimental results as well as the results from Mazellier & Vassilicos (2010)

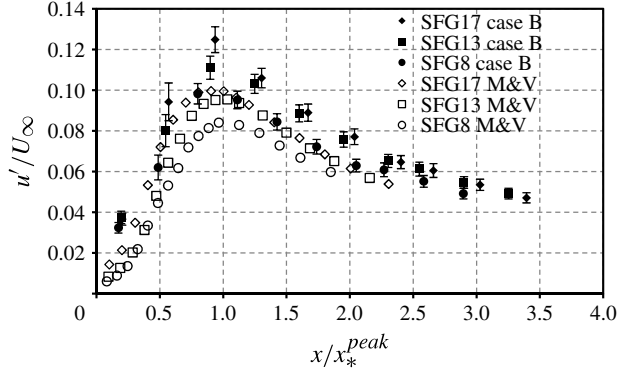


FIGURE 12. Streamwise evolution of the centreline non-normalized turbulence intensity as a function of x scaled by x_*^{peak} . Open symbols are data from Mazellier & Vassilicos (2010).

using U_∞ as the normalization scale. We choose x_*^{peak} to scale streamwise distance as it has already been shown that this parameter collapses the streamwise development of turbulence intensities. Figure 12 shows a lack of collapse of turbulence intensity data which is not within the experimental error.

Mazellier & Vassilicos (2010) have shown that the u'/U_∞ data in figure 12 can be collapsed by using the peak turbulence intensity. From (4.14), this peak turbulence intensity scales as $(1/\beta)\sqrt{C_d t_0/x_*^{peak}}$. Therefore, the scaling relation for the turbulence intensity is

$$\frac{u'}{U_\infty} = \frac{1}{\beta} \left(\frac{C_d t_0}{x_*^{peak}} \right)^{1/2} g \left(\frac{x}{x_*^{peak}}; * \right) \quad (4.15)$$

where the dimensionless function g depends on the streamwise distance x and the argument $*$ represents any dependences that might exist on boundary/inlet/initial conditions.

Figure 13 shows the streamwise development of the turbulence intensity with the streamwise distance scaled with x_*^{peak} and the turbulence intensity scaled according to (4.15). The collapse of the data appears to be very good, especially when compared to the scatter observed in figure 12. The collapse is relatively poorer near the peak turbulence intensity. This can be attributed to the uncertainty in the determination of C_d as well as β .

It is especially important to note that there is significant difficulty in accounting for the presence of free-stream turbulence in the scaling relations. The scatter, near the peak, in figure 13 is partly due to the presence of free-stream turbulence in the measurements obtained in the current study. Therefore, we now aim to examine this collapse in greater detail by only using data where the free stream is laminar. We use the fractal-grid data obtained using hot-wire anemometry in a wind tunnel (Mazellier & Vassilicos 2010) as well as the data obtained in the lee of regular grids (Groth & Johansson 1988; Cardesa-Dueñas *et al.* 2012). Details of the regular grids used in these two studies are in table 5.

Figure 14 shows the streamwise development of turbulence intensity for the three regular grids as well as for the fractal grids of Mazellier & Vassilicos (2010). The intensities are scaled using a β value of 8.3 (the value for laminar free stream). The

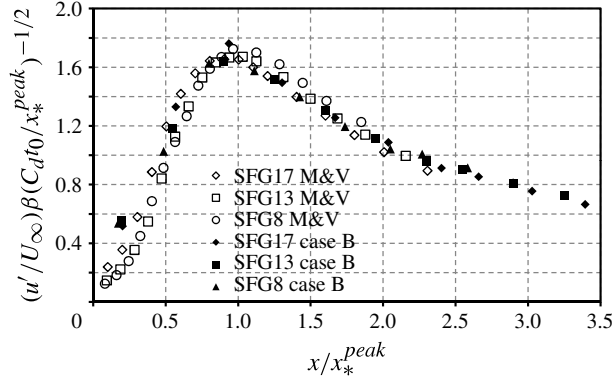


FIGURE 13. Streamwise evolution of the centreline turbulence intensity as a function of x scaled by x_*^{peak} . Turbulence intensity is normalized by relation (4.15). Open symbols are data from Mazellier & Vassilicos (2010).

Grid	Reference	Free-stream turb. int. (%)	Grid geom.	Solidity (%)	Mesh size, M (mm)	Thickness, t (mm)	Re_t
Sq34	Cardesa-Dueñas <i>et al.</i> (2012)	0.7	Square	34	32	6	3100
Rd44	Cardesa-Dueñas <i>et al.</i> (2012)	0.7	Round	44	32	8	4125
Mesh	Groth & Johansson (1988)	0.4	Round	35	5	1	330

TABLE 5. Regular-grid details.

Grid	Reference	C_d	α	ϕ	β
SFG8	Present study	2.40	0.287	0.21	7.2
SFG13	Present study	2.25	0.287	0.21	7.2
SFG17	Present study	2.10	0.287	0.21	7.2
SFG8	Mazellier & Vassilicos (2010)	2.18	0.231	0.21	8.3
SFG13	Mazellier & Vassilicos (2010)	2.12	0.231	0.21	8.3
SFG17	Mazellier & Vassilicos (2010)	2.09	0.231	0.21	8.3
Sq34	Cardesa-Dueñas <i>et al.</i> (2012)	2.19	0.231	0.16	8.3
Rd44	Cardesa-Dueñas <i>et al.</i> (2012)	1.2	0.280	0.16	8.3
Mesh	Groth & Johansson (1988)	1.1	0.210	0.16	8.3

TABLE 6. Coefficient values used in normalizations of the present study. The drag coefficients, C_d , are taken from Bearman & Trueman (1972) and Nakamura & Tomonari (1976) for values without and with free-stream turbulence, respectively.

collapse in figure 14 is not as good as in figure 13, specifically with the ‘Rd44’ data from Cardesa-Dueñas *et al.* (2012). However, it is encouraging to see that it is possible to predict the location of peak turbulence intensity and its magnitude regardless of the type of grid used. It is found that the better the estimate of the turbulence intensity peak location, the better the collapse of u'/U_∞ . However, the estimation of the peak location, determined by expression (4.5), does not hold for the regular grids because

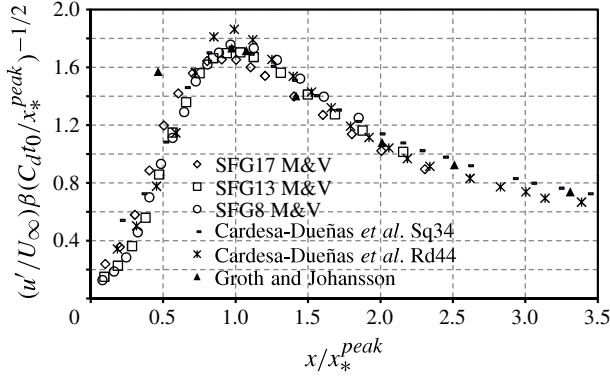


FIGURE 14. Streamwise evolution of the centreline turbulence intensity with the same normalization as figure 13. Besides the fractal-grid results from Mazellier & Vassilicos (2010), data from regular grids from Cardesa-Dueñas *et al.* (2012) are included, where ‘Sq34’ is related to the results of square bars and 34 % solidity and ‘Rd44’ is related to round bars and 44 % solidity; Groth & Johansson (1988) data include results from a mesh with round bars.

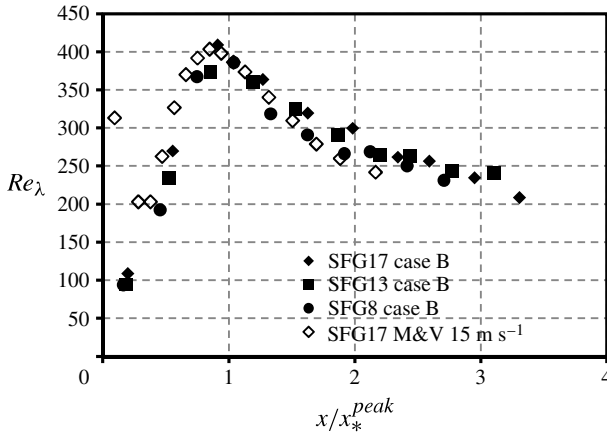


FIGURE 15. Re_λ as a function of x/x_*^{peak} along the centreline for the three fractal grids studied (case B) and comparison with the SFG17 data of Mazellier & Vassilicos (2010) for U_∞ of 15 m s^{-1} .

the coefficient ϕ that multiplies x_*' (see expression (4.5)) is not 0.21 but 0.16 for the regular grids considered here. Table 6 presents all coefficients used in the present paper to normalize data. The values of α for the round bars vary between 0.280 and 0.210 and were taken from Symes & Fink (1977) using the same methodology as in figure 9 (not presented here for brevity). Finally, it is interesting to observe that the scaling relations for the streamwise development of turbulence intensity in grid turbulence (both regular and fractal square grids) can be based on the turbulence characteristics of an isolated wake. This highlights the importance of pure wake flows and further detailed work is required to examine the turbulent characteristics of isolated wakes under different initial and boundary conditions, in particular incoming free-stream turbulence.

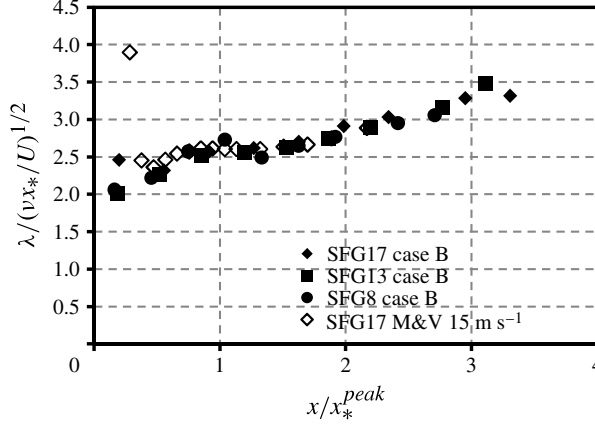


FIGURE 16. Taylor microscale, λ , normalized by $(vx_*/U)^{1/2}$, as a function of x/x_*^{peak} for the three fractal grids studied (case B) and comparison with the SFG17 data of Mazellier & Vassilicos (2010) for U_∞ of 15 m s^{-1} .

4.3. Comparison with HWA wind tunnel experiments

Figure 7(c) in §4.1 shows good agreement in turbulence intensity between the HWA measurements and the current PIV results provided the streamwise distance is normalized by x_*^{peak} . Therefore in all subsequent results we will use this new wake-interaction length scale to normalize streamwise distances.

Figure 15 shows the local Taylor Reynolds number, $Re_\lambda = u'\lambda/\nu$ (where the Taylor microscale, λ , is defined by $\sqrt{\langle u^2 \rangle / \langle (\partial u / \partial x)^2 \rangle}$), as a function of streamwise distance along the centreline. It can be seen that case B yields Re_λ comparable to the wind tunnel experiments at $U_\infty = 15 \text{ m s}^{-1}$. Despite some scatter in the decaying region, the data from these two different experiments exhibit similar behaviour. Even the peak of Re_λ appears at the same downstream distance and has the same magnitude in both experiments. Hence, the data of case B and the corresponding data for SFG17 and $U_\infty = 15 \text{ m s}^{-1}$ in Mazellier & Vassilicos (2010) are used from this point onwards to compare the results of the two experiments.

In terms of Taylor microscale, figure 16 shows an excellent agreement between the two different experiments. The Taylor microscale is normalized as in Mazellier & Vassilicos (2010) where they fitted an exponential law to the decaying turbulent region and derived that the turbulent energy dissipation should scale as $\epsilon \propto u'^2 U_\infty / x_*$. Using this expression and also $\epsilon \propto \nu u'^2 / \lambda^2$ it is possible to arrive at the following normalization used in figure 16:

$$\frac{u'^2 U_\infty}{x_*} \propto \frac{\nu u'^2}{\lambda^2} \Leftrightarrow \lambda \sqrt{\frac{U_\infty}{\nu x_*}} \propto \text{constant}. \quad (4.16)$$

Figure 16 shows that the Taylor microscale can be collapsed in terms of $\sqrt{\nu x_* / U_\infty}$ but that it is not exactly constant as x/x_*^{peak} is varied. This deviation from $\lambda \sqrt{U_\infty / \nu x_*} \propto \text{constant}$ was noted by Mazellier & Vassilicos (2010) and reflects the fact that the turbulence decay is in fact not exponential but a fast power law which can be fitted quite closely by an exponential for some distance downstream (see Mazellier & Vassilicos 2010; Valente & Vassilicos 2011a).

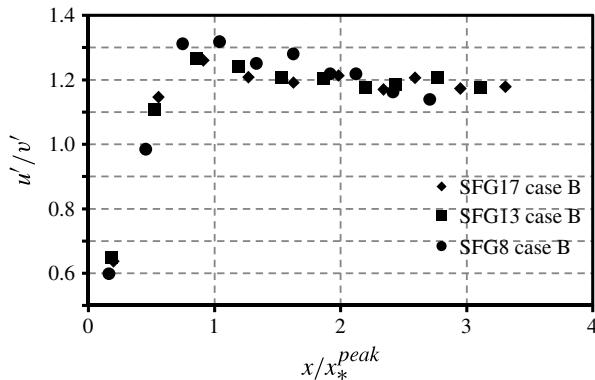


FIGURE 17. Global isotropy parameter u'/v' as a function of the distance downstream of the fractal grids for case B.

Figures 7, 15 and 16 show that it is possible to recover the same behaviour and results from two different experimental facilities such as a wind tunnel and water tunnel and two different experimental techniques such as hot-wire anemometry and PIV. In addition, comparable results are obtained even with a substantial free-stream turbulence in the incoming flow. The only difference between the two experiments compared here is the turbulence intensity of the incoming flow, which alters the wake growth from the grid bars and therefore the turbulence intensity peak appears earlier in the results obtained in the current study. However, by using appropriate scaling relations that account for incoming free-stream turbulence, the data from different experiments can be collapsed. This suggests that the turbulence generated by space-filling fractal square grids exhibits similar behaviour in our flume, which has significant background turbulence, as in wind tunnel experiments where the background turbulence is negligible even though, as we report in §4.5.1, the background turbulence in our facility has a similar integral length scale to the turbulence generated by our fractal grids.

4.4. Global and local isotropy

Isotropic turbulence was first studied by Taylor (1935) and it is characterized by the constancy of the statistical quantities in relation to rotations and reflections about all axes. The assumption of isotropy implies that it is only necessary to measure the velocity gradient in one direction in order to determine kinetic energy dissipation.

Before delving into small scales or local isotropy it is useful to look at large scales or global isotropy. Figure 17 shows the variation with downstream distance of the ratio of root-mean-square (r.m.s.) velocities in the streamwise and spanwise directions u'/v' . The streamwise distance is normalized by x_*^{peak} . This figure shows that for most downstream locations and for all three grids studied, u'/v' is slightly smaller than 1.2. This is in agreement with the results of Hurst & Vassilicos (2007) where a similar value for this ratio was found at locations that are sufficiently far downstream of the peak in turbulence intensity. In the aforementioned paper the authors acknowledged the importance of comparing results from different grids by normalizing them with x_{peak} (the distance where the turbulence intensity peaks) and presented a good collapse between their grids.

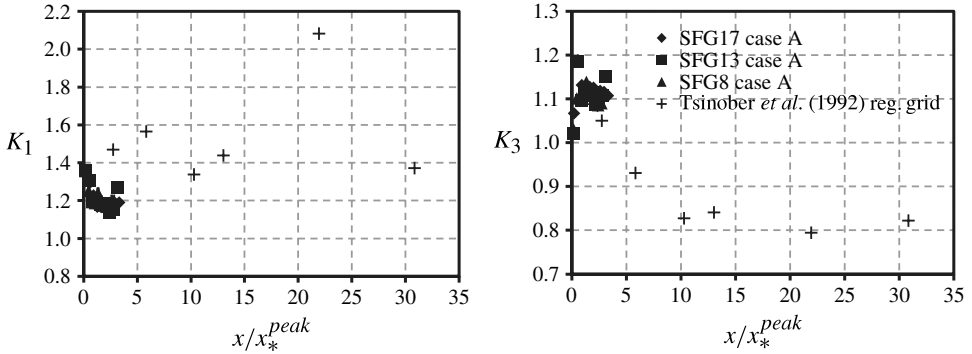


FIGURE 18. Local isotropy parameters K_1 and K_3 as a function of the distance downstream of the fractal grids for case A compared with the results from Tsinober *et al.* (1992) for a regular grid.

In terms of small-scale or local isotropy, it is very difficult to generate a flow where the velocity gradient statistics are invariant to reflections and rotations about all axes. Several examples of local isotropy studies can be found in George & Hussein (1991) who adapted the results of Browne, Antonia & Shah (1987) for different types of turbulence sources (wakes, jets, pipes, etc.) with the exception of grid turbulence.

According to Kolmogorov's first hypothesis of similarity, the small scales are supposedly locally isotropic if the Reynolds number is high enough. The small scales are largely responsible for the behaviour of the velocity derivatives and hence it is thought that the relations derived by Taylor (1935) hold, that is the ratios

$$K_1 = 2 \left\langle \left(\frac{\partial u}{\partial x} \right)^2 \right\rangle / \left\langle \left(\frac{\partial v}{\partial x} \right)^2 \right\rangle, \quad K_3 = 2 \left\langle \left(\frac{\partial u}{\partial x} \right)^2 \right\rangle / \left\langle \left(\frac{\partial u}{\partial y} \right)^2 \right\rangle \quad (4.17)$$

should be equal to 1. In the present study, we only report on two ratios (K_1 and K_3). This is because we can only determine these two ratios from our planar PIV measurements.

Figure 18 shows variation in K_1 and K_3 with streamwise distance. It should be noted that we only show the data from case A for the sake of clarity; however, all the other cases have very similar values of K_1 and K_3 . The figure also shows data from a regular grid taken from Tsinober, Kit & Dracos (1992). The regular grid in their study was made of round rods (15 mm diameter) arranged in a square mesh with a mesh size of 60 mm. The solidity of their grid was 0.44 and the free-stream velocity was 7 m s^{-1} . The Re_0 of their study was comparable to the Re_0 of case A in the current study (see definition of Re_0 in table 1). In order to compare results from the two different experiments, the turbulence intensity peak is estimated for the regular grid using (4.5) as it was not captured in the experiments of Tsinober *et al.* (1992). It can be seen in figure 18 that local isotropy parameters do not tend to unity for both fractal and regular grids. This is consistent with the observations of Browne *et al.* (1987) and George & Hussein (1991) who reported similar findings in other types of turbulent flows. However, there is no significant difference in local isotropy parameters between the fractal and regular grids in the region x/x_*^{peak} where we have one data point for comparison from the Tsinober *et al.* (1992) regular grid study.

4.5. Energy dissipation scaling

It is considered a cornerstone assumption in turbulence theory (see Townsend 1956; Tennekes & Lumley 1972; Pope 2000) that when the Reynolds number is high enough, turbulent energy dissipation scales as

$$\epsilon = C_\epsilon \frac{u'^3}{L} \quad (4.18)$$

where u' is the r.m.s. of the velocity fluctuations, L is an integral length scale and C_ϵ is a constant independent of space, time and Re . In Burattini, Lavoie & Antonia (2005), for example, it is possible to see that the C_ϵ constancy for high Re is even found in some inhomogeneous types of flow such as wakes and jets.

Looking at the Richardson–Kolmogorov cascade phenomenology, the small scales do not directly feel the large scales whose characteristics depend mainly on the mechanism that generates the turbulence in the first place. It is then assumed that the energy dissipated by the small scales is transferred by the cascade, from the large scales. Hence, the scaling of turbulent energy dissipation should be a ratio between u'^2 , effectively the turbulent kinetic energy, and L/u' which is the time for the energy to cascade until dissipation. As clearly stated by Batchelor (1953) this cascade phenomenology is expected to be valid for a wide range of turbulent flows, not only perfectly homogeneous isotropic turbulence.

Therefore, if we consider the aforementioned scaling for energy dissipation together with an estimation of the Taylor microscale given by $\epsilon \propto \nu u'^2/\lambda^2$, then the following expression can be derived:

$$\frac{L}{\lambda} \propto Re_\lambda. \quad (4.19)$$

Relation (4.19) is the result of considering C_ϵ as a constant and it depicts the well-known phenomenon that an increase in the Reynolds number causes the range of excited turbulent scales to increase too. In order to verify if the flow in the present study follows relation (4.19) it is necessary to estimate an integral length scale. The following subsection looks at means of doing this from our PIV data.

4.5.1. Integral length scale estimation

The integral length scale is obtained by computing the longitudinal correlation function $f(r, x) = \overline{u(x)u(x+r)}/\overline{u(x)^2}$. Figure 19(a) shows the streamwise variation of the correlation function for the SFG17 grid (case B). The correlation does not reach zero with our field of view. Therefore, our large-scale field of view is not sufficient to capture this information. However, we can estimate the integral scale by fitting a function to the data and integrating this function.

In order to confirm that fitting a function to the data will result in a good estimation of the integral length scale, data from the present study are compared with the results of Discetti *et al.* (2011) who performed high-resolution planar PIV measurements in the wake of similar fractal square grids. Measurements in the current study as well in Discetti *et al.* (2011) are taken in the same region of the flow, at around $x/x_*^{peak} \approx 1.3$.

Figure 19(b) shows a comparison between the streamwise autocorrelation obtained by Discetti *et al.* (2011) and the current study. It can be seen that the data from the two studies are in excellent agreement. Since the study by Discetti *et al.* (2011) has a longer field of view, we can compare the fit to the correlation obtained using our data to the data from Discetti *et al.* (2011). This in turn will validate the fitting function and hence our estimate of the integral length scale. Figure 19(c) shows the data from

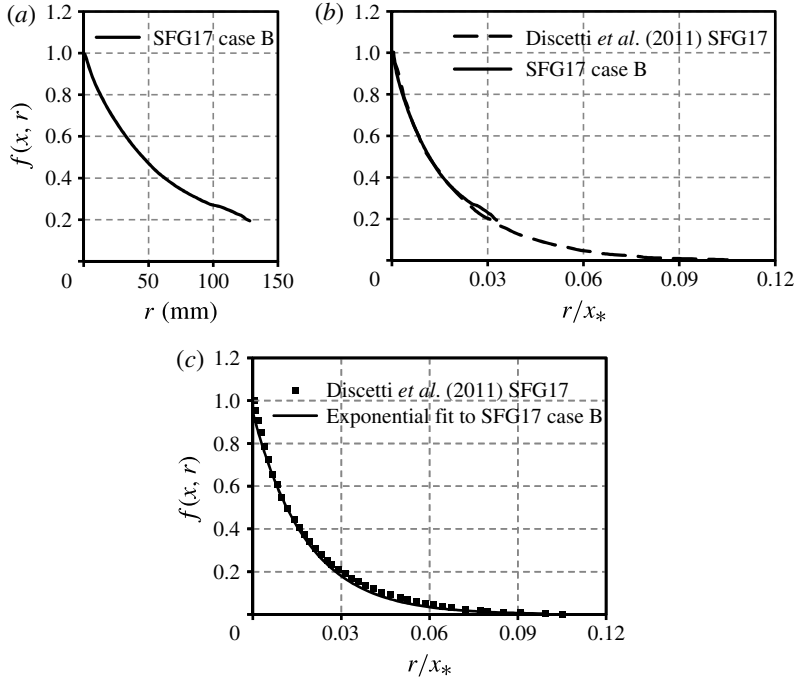


FIGURE 19. Longitudinal correlation function (a) at $x/x_*^{peak} \approx 1.3$ for the SFG17 grid and case B; (b) with the addition of data from Discetti *et al.* (2011) for a fractal grid SFG17 at $x/x_*^{peak} \approx 1.3$ normalized by x_* ; and (c) with the addition of an exponential fit for the data of the present study SFG17 case B.

Discetti *et al.* (2011) as well the exponential fit obtained from the data in the current study. The fit appears to be an excellent approximation to the experimental data. Therefore, the integral length scale will be calculated by integrating the exponential fit and this scale will be used in subsequent sections.

The integral length scale of the free-stream turbulence when $U_\infty = 0.59 \text{ m s}^{-1}$, as in case B, is estimated using the same aforementioned procedure and takes the value $L_u \approx 0.2L_0$ (where $L_0 \approx 303 \text{ mm}$) at the first station of measurements (0.3 m downstream of where the grid would sit). This is comparable with the integral length scale values produced by our grids which range from $L_u/L_0 \approx 0.15$ close to the grid to 0.3 at the last stations of measurements.

4.5.2. Energy dissipation scaling results

As mentioned before, the dependence of L/λ on Re_λ is a way to check the energy dissipation scaling in (4.18). If it is found that L/λ and Re_λ decay together with increasing x/x_*^{peak} such that $L/\lambda \propto Re_\lambda$ then (4.18) holds with constant C_ϵ . Figure 20(a) shows the ratio of the integral length scale L_u to the Taylor microscale λ as a function of downstream distance. It is possible to see that L_u/λ does not change significantly with x for the distances covered in this study. This would not be important if the Reynolds number remained constant. However, figure 15 shows that the Reynolds number in fact decreases with increasing streamwise distance beyond $x/x_*^{peak} \approx 1$. This suggests that the flow in the decaying region of the turbulent flow generated by the fractal square grid does not conform with the scaling (4.18).

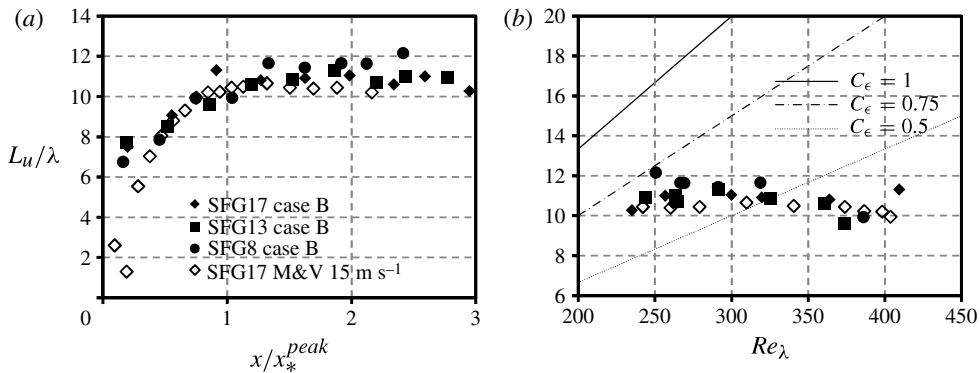


FIGURE 20. Integral to Taylor microscale ratio L_u/λ for case B and results from Mazellier & Vassilicos (2010) in relation to (a) x/x_*^{peak} and (b) Re_λ .

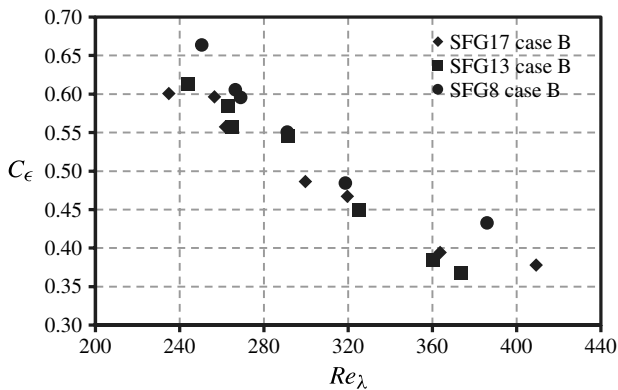


FIGURE 21. Energy dissipation parameter C_ϵ in relation to Re_λ for the fractal grids studied.

Figure 20(b) is perhaps a better way of visualizing this unusual behaviour by plotting the ratio L_u/λ as a function of Re_λ and showing that L_u/λ remains approximately constant as Re_λ changes. In this figure there is a reasonable agreement between the results from the present study and those of Mazellier & Vassilicos (2010) in spite of the difficulty of measuring integral length scales.

Therefore, for the present case, as previously reported by Seoud & Vassilicos (2007), Mazellier & Vassilicos (2010) and Valente & Vassilicos (2011a), the scaling in (4.18) does not hold. This is primarily because C_ϵ is not a constant in the region of the fractal-generated turbulent flows studied here. In fact, Seoud & Vassilicos (2007), Mazellier & Vassilicos (2010) and Valente & Vassilicos (2011a) showed that C_ϵ increases with global Reynolds number Re_0 and is inversely proportional to the local Reynolds number Re_λ . This observation is confirmed in figure 21 where it can be seen that C_ϵ decreases with increasing Re_λ .

5. Conclusions

In the present paper we report on an investigation of the flow in the lee of space-filling square fractal grids in a water tunnel using planar PIV. The main contribution

of this paper is the introduction of an improved and generalized wake interaction length scale and a turbulence intensity scaling which, together, collapse the data from different experiments with different grids (fractal/multiscale and regular) with and without incoming turbulence intensity. Moreover, data from hot-wire anemometry experiments carried out in a wind tunnel (mainly from Mazellier & Vassilicos 2010) were also compared with the present study, as were the local and global isotropy parameters from our current study to those obtained with regular grids in other studies.

When the incoming flow has free-stream turbulence, the wakes developing downstream of the grids have a higher rate of growth compared to a flow with laminar incoming flow. This has consequence in the magnitude of turbulence intensity produced by the grid and the location where the turbulence peaks. The wake development was taken into account in our investigation through the introduction of a new wake-interaction length scale (x_*^{peak}). This length scale requires information about development of an isolated wake in the presence of free-stream turbulence, which was taken from previously published results (see Symes & Fink 1977). This new wake-interaction length scale takes into account the free-stream turbulence characteristics and the geometry of the grid. It also provides an estimation of the turbulence intensity peak location. In addition to the wake-interaction length scale, we also demonstrate that the turbulence intensity scales with wake velocity deficit by using the streamwise momentum equation (together with certain assumptions). This, together with our new wake-interaction length scale, allowed us to derive a scaling relation for turbulence intensity which seems valid both for regular and fractal square-grid-generated turbulence.

In terms of isotropy, it was found that both global and local parameters are consistent with previous studies in the literature. The ratio of u'/v' is close to 1.2 beyond $x/x_*^{peak} \approx 2$. The parameters K_1 and K_3 (see (4.17)) are found to be 1.2 and 1.1, respectively, which is also consistent with results obtained in regular grid experiments, suggesting that there is no significant difference in local isotropy parameters across these different flows in the flow regions considered.

Finally, the energy dissipation scaling was revisited in our investigation and it was confirmed that the ratio L_u/λ remains approximately constant while the Reynolds number decreases in the streamwise region between x_*^{peak} and $3x_*^{peak}$. This is a very long region in our experiments where x_*^{peak} , for the grid SFG17, is approximately 1.4 m. Hence, (4.18) with $C_\epsilon \approx \text{constant}$ is not valid in this region. Instead, $C_\epsilon \propto 1/Re_\lambda$.

Acknowledgements

We gratefully acknowledge the financial support from EPSRC through Grant No. EP/H030875/1. We also acknowledge the technicians in the Department of Aeronautics workshop for all their help with setting up the experiments.

REFERENCES

- ADRIAN, R. J. & WESTERWEEL, J. 2011 *Particle Image Velocimetry*. Cambridge University Press.
- ALY, A., ABOU, E.-A., CHONG, A., NICOLLEAU, F. & BECK, S. 2010 Experimental study of the pressure drop after fractal-shaped orifices in turbulent pipe flows. *Exp. Therm. Fluid Sci.* **34** (1), 104–111.
- ANDERSON, W. & MENEVEAU, C. 2011 Dynamic roughness model for large-eddy simulation of turbulent flow over multiscale, fractal-like rough surfaces. *J. Fluid Mech.* **679**, 288–314.
- ANTONIA, R. A., ZHOU, T. & ROMANO, G. P. 2002 Small-scale turbulence characteristics of two-dimensional bluff body wakes. *J. Fluid Mech.* **459**, 67–92.

- BAI, K., MENEVEAU, C. & KATZ, J. 2012 Near-wake turbulent flow structure and mixing length downstream of a fractal tree. *Boundary-Layer Meteorol.* **143**, 285–308.
- BATCHELOR, G. K. 1953 *The Theory of Homogeneous Turbulence*. Cambridge University Press.
- BEARMAN, P. W. & TRUEMAN, D. M. 1972 An investigation of the flow around rectangular cylinders. *Aeronaut. Q.* **23**, 229–237.
- BIFERALE, L., CENCINI, M., LANOTTE, A. S., SBRAGAGLIA, M. & TOSCHI, 2004 Anomalous scaling and universality in hydrodynamic systems with power-law forcing. *New J. Phys.* **6**, 37.
- BROWNE, L. W. B., ANTONIA, R. A. & SHAH, D. A. 1987 Turbulent energy dissipation in a wake. *J. Fluid Mech.* **179**, 307–326.
- BURATTINI, P., LAVOIE, P. & ANTONIA, R. A. 2005 On the normalized turbulent energy dissipation rate. *Phys. Fluids* **17**, 098103.
- BUXTON, O. R. H. 2011 Fine scale features of turbulent shear flows. PhD thesis, Imperial College London.
- CARDESA-DUEÑAS, J. I., NICKELS, T. B. & DAWSON, J. R. 2012 2D PIV measurements in the near field of grid turbulence using stitched fields from multiple cameras. *Exp. Fluids* **52**, 1611–1627.
- CHESKIDOV, A. & DOERING, C. R. 2007 Energy dissipation in fractal-forced flow. *J. Math. Phys.* **48**, 065208.
- CHESTER, S. & MENEVEAU, C. 2007 Renormalized numerical simulation of flow over planar and non-planar fractal trees. *Environ. Fluid Mech.* **7**, 280–301.
- CHESTER, S., MENEVEAU, C. & PARLANGE, M. B. 2007 Modeling turbulent flow over fractal trees with renormalized numerical simulation. *J. Comput. Phys.* **225** (1), 427–448.
- DALLAS, V., VASSILICOS, J. C. & HEWITT, G. F. 2009 Stagnation point von Karman coefficient. *Phys. Rev. E* **80**, 046306.
- DISCETTI, S., ZISKIN, I. B., ADRIAN, R. J. & PRESTRIDGE, K. 2011 PIV study of fractal grid turbulence. In *9th International Symposium on Particle Image Velocimetry – PIV'11, Kobe, Japan*. Visualization Society of Japan.
- DOERING, C. R. & FOIAS, C. 2002 Energy dissipation in body-forced turbulence. *J. Fluid Mech.* **467**, 289–306.
- EAMES, I., JONSSON, C. & JOHNSON, P. B. 2011 The growth of a cylinder wake in turbulent flow. *J. Turbul.* **12**, 1–16.
- GEIPEL, P., GOH, K. H. H. & LINDSTEDT, R. P. 2010 Fractal-generated turbulence in opposed jet flows. *Flow Turbul. Combust.* **85** (3–4), 397–419.
- GEORGE, W. K. 1992 The decay of homogeneous turbulence. *Phys. Fluids A* **4**, 1492.
- GEORGE, W. K. & HUSSEIN, H. J. 1991 Locally axisymmetric turbulence. *J. Fluid Mech.* **233**, 1–23.
- GROTH, J. & JOHANSSON, A. V. 1988 Turbulence reduction by screens. *J. Fluid Mech.* **197**, 139–155.
- HOPFINGER, E. J. & TOLY, J. A. 1976 Spatially decaying turbulence and its relation to mixing across density interfaces. *J. Fluid Mech.* **78**, 155–175.
- HURST, D. & VASSILICOS, J. C. 2007 Scalings and decay of fractal-generated turbulence. *Phys. Fluids* **19**, 035103.
- KANG, H. K., DENNIS, D. & MENEVEAU, C. 2011 Flow over fractals: drag forces and near wakes. *Fractals* **19**, 387–399.
- KEYLOCK, C. J., NISHIMURA, K., NEMOTO, M. & ITO, Y. 2012 The flow structure in the wake of a fractal fence and the absence of an inertial regime. *Environ. Fluid Mech.* **12**, 227–250.
- KINZEL, M., WOLF, M., HOLZNER, M., LÜTHI, B., TROPEA, C. & KINZELBACH, W. 2011 Simultaneous two-scale 3D-PTV measurements in turbulence under the influence of system rotation. *Exp. Fluids* **51** (1), 75–82.
- KUCZAJ, A. K. & GEURTS, B. J. 2006 Mixing in manipulated turbulence. *J. Turbul.* **7**, 1–35.
- KUCZAJ, A. K., GEURTS, B. J. & MCCOMB, W. D. 2006 Non local modulation of the energy cascade in broadband-forced turbulence. *Phys. Rev. E* **74**, 016306.
- LAIZET, S., FORTUNÉ, V., LAMBALLAIS, V. & VASSILICOS, J. C. 2012 Low Mach number prediction of the acoustic signature of fractal-generated turbulence. *Intl J. Heat Fluid Flow* **35**, 25–32.

- LAISET, S., LAMBALLAIS, E. & VASSILICOS, J. C. 2010 A numerical strategy to combine high-order schemes, complex geometry and parallel computing for high resolution dns of fractal generated turbulence. *Comput. Fluids* **39** (3), 471–484.
- LAISET, S. & VASSILICOS, J. C. 2011 DNS of fractal-generated turbulence. *Flow Turbul. Combust.* **87**, 673–705.
- LAISET, S. & VASSILICOS, J. C. 2012 The fractal space-scale unfolding mechanism for energy-efficient turbulent mixing. *Phys. Rev. Lett.* (submitted).
- MAZELLIER, N. & VASSILICOS, J. C. 2008 The turbulence dissipation constant is not universal because of its universal dependence on large-scale flow topology. *Phys. Fluids* **20**, 014102.
- MAZELLIER, N. & VASSILICOS, J. C. 2010 Turbulence without Richardson–Kolmogorov cascade. *Phys. Fluids* **22**, 075101.
- MAZZI, B., OKKELS, F. & VASSILICOS, J. C. 2002 A shell-model approach to fractal-induced turbulence. *Eur. J. Mech. (B/Fluids)* **28** (2), 231–241.
- MAZZI, B. & VASSILICOS, J. C. 2004 Fractal-generated turbulence. *J. Fluid Mech.* **502**, 65–87.
- NAGATA, K., SUZUKI, H., SAKAI, H., HAYASE, Y. & KUBO, T. 2008a Direct numerical simulation of turbulence characteristics generated by fractal grids. *Intl Rev. Phys.* **5**, 400–409.
- NAGATA, K., SUZUKI, H., SAKAI, H., HAYASE, Y. & KUBO, T. 2008b Direct numerical simulation of turbulent mixing in grid-generated turbulence. *Phys. Scr.* **132**, 014054.
- NAKAMURA, Y. & TOMONARI, Y. 1976 The effect of turbulence on the drags of rectangular prisms. *Trans. Japan Soc. Aeronaut. Space Sci.* **19**, 81–86.
- NEDIC, J., GANAPATHISUBRAMANI, B., VASSILICOS, J. C., BOREE, J., BRIZZI, L. E. & SPOHN, A. 2012 Aero-acoustic performance of fractal spoilers. *AIAA J.* (in press).
- NICOLLEAU, F., SALIM, S. & NOWAKOWSKI, A. F. 2011 Experimental study of a turbulent pipe flow through a fractal plate. *J. Turbul.* **12**, 1–20.
- POPE, S. B. 2000 *Turbulent Flows*. Cambridge University Press.
- QUEIROS-CONDE, D. & VASSILICOS, J. C. 2001 Turbulent wakes of 3-D fractal grids. In *Intermittency in Turbulent Flows and Other Dynamical Systems* (ed. J. C. Vassilicos). Cambridge University Press.
- SAARENINNE, P. & PIIRTO, M. 2000 Turbulent kinetic energy dissipation rate estimation from PIV vector fields. *Exp. Fluids* **29**, S300–S307.
- SEOUD, R. E. & VASSILICOS, J. C. 2007 Dissipation and decay of fractal-generated turbulence. *Phys. Fluids* **19**, 105108.
- SOLOFF, S. M., ADRIAN, R. J. & LIU, Z.-C. 1997 Distortion compensation for generalized stereoscopic particle image velocimetry. *Meas. Sci. Technol.* **8**, 1441–1454.
- STAIKU, A., MAZZI, B., VASSILICOS, J. C. & VAN DE WATER, W. 2003 Turbulent wakes of fractal objects. *Phys. Rev. E* **67** (6), 066306.
- STRESING, R., PEINKE, J., SEOUD, R. E. & VASSILICOS, J. C. 2010 Defining a new class of turbulent flows. *Phys. Rev. Lett.* **104**, 194501.
- SUZUKI, H., NAGATA, K., SAKAI, Y. & UKAI, R. 2010 High-Schmidt-number scalar transfer in regular and fractal grid turbulence. *Phys. Scr.* **T142**, 014069.
- SYMES, C. R. & FINK, L. E. 1977 Effects of external turbulence upon the flow past cylinders. In *Structure and Mechanisms of Turbulence I* (ed. H. Fiedler), pp. 86–102. Springer.
- TANAKA, T. & EATON, J. K. 2007 A correction method for measuring turbulence kinetic energy dissipation rate by PIV. *Exp. Fluids* **42**, 893–902.
- TAYLOR, G. I. 1935 Statistical theory of turbulence. *Proc. R. Soc. Lond. A* **151**, 421–478.
- TENNEKES, H. & LUMLEY, J. L. 1972 *A First Course in Turbulence*. MIT.
- TOWNSEND, A. A. 1956 *The Structure of Turbulent Shear Flows*. Cambridge University Press.
- TSINOBER, A., KIT, E. & DRACOS, T. 1992 Experimental investigation of the field of velocity gradients in turbulent flows. *J. Fluid Mech.* **242**, 169–192.
- VALENTE, P. C. & VASSILICOS, J. C. 2011a The decay of turbulence generated by a class of multi-scale grids. *J. Fluid Mech.* **687**, 300–340.
- VALENTE, P. C. & VASSILICOS, J. C. 2011b Comment on dissipation and decay of fractal-generated turbulence [Phys. Fluids 19, 105108 (2007)]. *Phys. Fluids* **23**, 119101.

- VALENTE, P. C. & VASSILICOS, J. C. 2012*a* Dependence of decaying homogeneous isotropic turbulence on inflow conditions. *Phys. Lett. A* **376**, 510–514.
- VALENTE, P. C. & VASSILICOS, J. C. 2012*b* Universal dissipation scaling for non-equilibrium turbulence. *Phys. Rev. Lett.* **108**, 214503.
- WYGNANSKI, I., CHAMPAGNE, F. & MARASLI, B. 1986 On the large-scale structures in two-dimensional, small-deficit, turbulent wakes. *J. Fluid Mech.* **168**, 31–71.
- ZHENG, H. W., NICOLLEAU, F. & QIN, N. 2012 Detached eddy simulation for turbulent flows in a pipe with a snowflake fractal orifice. In *New Approaches in Modeling Multiphase Flows and Dispersion in Turbulence, Fractal Methods and Synthetic Turbulence* (ed. F. C. G. A. Nicolleau, C. Cambon, J.-M. Redondo, J. C. Vassilicos, M. Reeks & A. F. Nowakowski). Springer.